Annual Review of Physical Chemistry

Studies of Local DNA Backbone Conformation and Conformational Disorder Using Site-Specific Exciton-Coupled Dimer Probe Spectroscopy

Andrew H. Marcus,[1,2,3,4] Dylan Heussman,[1,2,3]
Jack Maurer,[1,2,3] Claire S. Albrecht,[1,2,4]
Patrick Herbert,[1,2,3] and Peter H. von Hippel[2,3]

[1] Center for Optical, Molecular and Quantum Science, University of Oregon, Eugene, Oregon, USA; email: ahmarcus@uoregon.edu

[2] Institute of Molecular Biology, University of Oregon, Eugene, Oregon, USA

[3] Department of Chemistry and Biochemistry, University of Oregon, Eugene, Oregon, USA

[4] Department of Physics, University of Oregon, Eugene, Oregon, USA

Annu. Rev. Phys. Chem. 2023. 74:245–65

First published as a Review in Advance on
January 25, 2023

The *Annual Review of Physical Chemistry* is online at
physchem.annualreviews.org

https://doi.org/10.1146/annurev-physchem-090419-041204

Keywords

exciton-coupled dimers, 2D spectroscopy, protein–DNA interactions, DNA replication, site-specific fluorescence labeling, DNA breathing

Abstract

The processes of genome expression, regulation, and repair require direct interactions between proteins and DNA at specific sites located at and near single-stranded–double-stranded DNA (ssDNA–dsDNA) junctions. Here, we review the application of recently developed spectroscopic methods and analyses that combine linear absorbance and circular dichroism spectroscopy with nonlinear 2D fluorescence spectroscopy to study the local conformations and conformational disorder of the sugar-phosphate backbones of ssDNA–dsDNA fork constructs that have been internally labeled with exciton-coupled cyanine $(iCy3)_2$ dimer probes. With the application of these methods, the $(iCy3)_2$ dimer can serve as a reliable probe of the mean local conformations and conformational distributions of the sugar-phosphate backbones of dsDNA at various critical positions. The results of our studies suggest a possible structural framework for understanding the roles of DNA breathing in driving the processes of protein–DNA complex assembly and function.

1. INTRODUCTION

Chemically driven biological processes are often described in terms of site-specific macromolecular interactions (1–3). In this review, we discuss recently developed spectroscopic methods and analyses that utilize the unique optical properties of exciton-coupled dimer probes to reveal detailed structural information about site-specific interactions within DNA and protein–DNA complexes. Among the most biologically significant protein–DNA interactions are those that guide the assembly and expression of the DNA genome (4). The interlocked processes that carry out these functions include DNA replication, recombination, and repair and DNA-directed RNA transcription. All these reactions involve (*a*) the replication of both strands of the paternal DNA duplex genome from its constituent single-stranded DNA (ssDNA) templates to produce two daughter duplex genomes of identical sequence; (*b*) processes that carry out DNA proofreading and repair activities when replication goes astray (because, while the initial template-directed synthesis of chromosomes proceeds with very high accuracy, thermodynamics requires that such processes cannot be completed with perfect fidelity); and (*c*) the copying of specific DNA sequences into messenger RNA sequences (transcription) that code for proteins (translation). In the following sections, we illustrate approaches to understanding the molecular mechanisms of these processes by applying these methodologies to study site-specific protein–DNA interactions within the replication complex (replisome) of the bacteriophage T4, which is the simplest organism that uses the replication components (subassemblies) that are also used for replication by essentially all higher organisms, from bacteria to humans. Thus, the T4 replisome, which is devoid of many of the regulatory complications that control the replication systems of higher organisms, provides an excellent model system to study the core functions of DNA synthesis.

1.1. The T4 DNA Replisome as a Model System for the Study of Protein–DNA Assembly and Interaction Mechanisms

The T4 bacteriophage replisome is a multisubunit complex whose individual protein components act in concert (i.e., cooperatively) to carry out the complex biochemical reactions of template-directed DNA synthesis. **Figure 1*a*** illustrates the molecular functions of the T4 replisome in the elongation phase of template-driven DNA synthesis (5). The core functional elements of the replisome compose three protein–DNA subassemblies: (*a*) The primase–helicase (primosome) complex utilizes the chemical free energy of ATP hydrolysis to drive the controlled opening of the native DNA duplex to expose the ssDNA template strands. (*b*) The ssDNA template strands are used by the DNA polymerases of the replication elongation complex to catalyze the template-directed DNA synthesis of the two complementary nascent daughter strands from free nucleotide triphosphate precursors present in solution. (*c*) The processivity clamps and clamp–loader complexes, by tethering (and untethering) the DNA polymerases to and from the template ssDNA strands, control the processivity[1] of the DNA replication process in both

---

[1] The processivity of the DNA polymerase is defined as the number of nucleotide residues added to the nascent chain per polymerase binding event. Under physiological conditions, and in the absence of the clamp, the

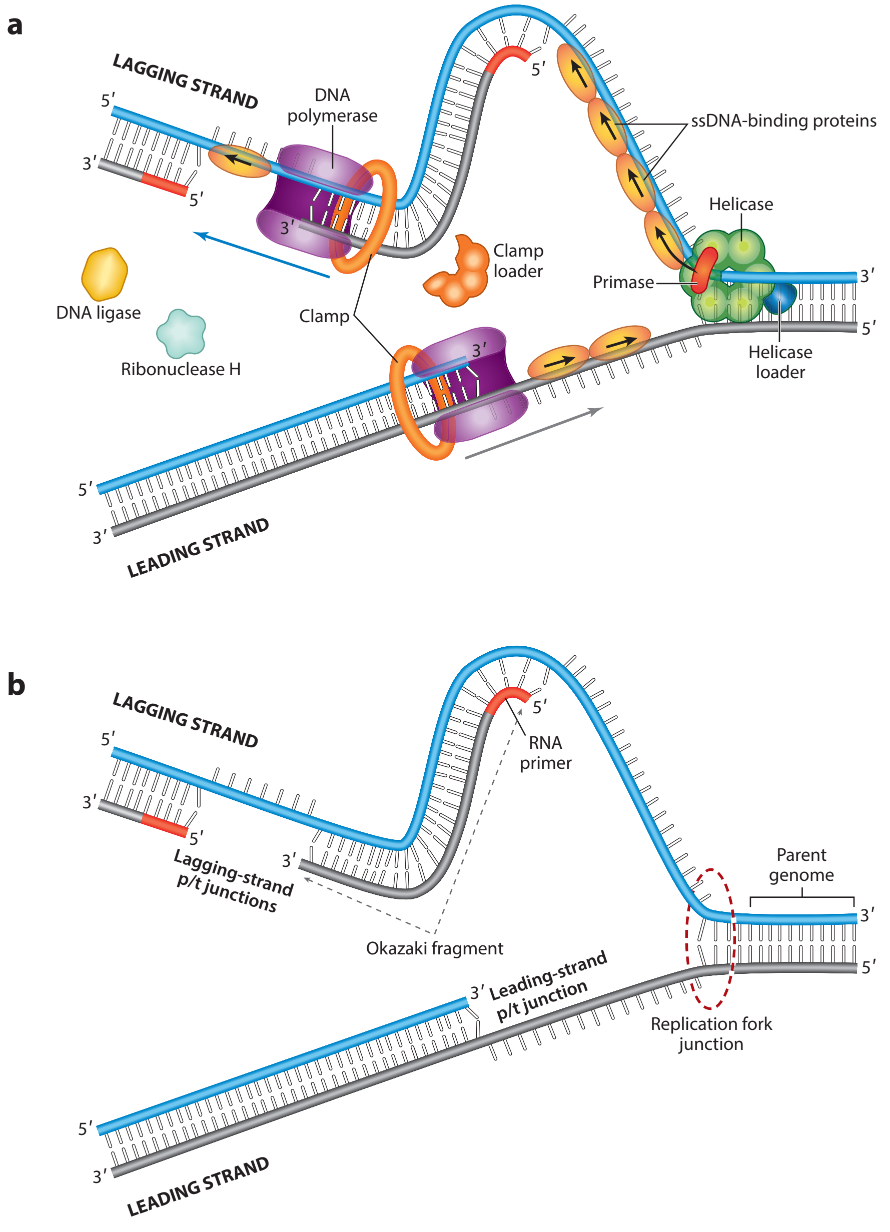

Figure 1

Schematic views of the T4 bacteriophage DNA replication complex with (*a*) and without (*b*) its protein components. Figure adapted from Reference 5.

---

polymerase adds only approximately one nucleotide residue to either nascent strand before dissociating, and when the clamp is loaded onto the polymerase the latter becomes essentially fully processive; that is, it synthesizes to the end of the template strand in leading-strand synthesis or until it encounters the 5′-end of another nascent DNA strand in lagging-strand synthesis (for context, see **Figure 1*a***).

leading- and lagging-strand DNA synthesis. The global conformation of the replisome in its elongation phase, shown in **Figure 1*a***, is often referred to as the trombone model, reflecting the growing loop structure of the lagging-strand fragments (6, 7). The trombone model was first proposed by Alberts (6) to explain topologically how the synthesis of the two nascent strands can proceed in synchrony in the same direction along the DNA duplex, even though, as enzymes, the polymerases can catalyze synthesis only in the 5′ to 3′ direction of the (chemically) antiparallel complementary template strands of the parental DNA duplex.

Thus, the shape of the replisome permits synthesis of the two nascent strands to proceed simultaneously in opposite (chemical) directions while allowing the overall replication process to proceed within a single functional complex. However, as a consequence (and as pointed out above), the processivity of leading- and lagging-strand DNA synthesis must differ, with the nascent leading strand being synthesized continuously whereas synthesis on the lagging strand must be discontinuous and involves both different processivity controls and periodic (RNA-primed) reinitiation of the synthesis of the shorter DNA (so-called Okazaki) fragments required to make lagging-strand DNA synthesis work (8) (see **Figure 1*a***). The ssDNA-binding proteins (also shown in **Figure 1*a***) manipulate the conformations of the ssDNA templates into their optimal configurations for synthesis, protect them from cleavage by single-strand-specific DNA nucleases, and integrate, in coordination with additional regulatory proteins, the interactions of the three functional subassemblies of the T4 replisome described above (9, 10).

During DNA replication in the elongation phase, individual protein components of the replisome form quasi-stable subassemblies, which are bound to the framework of the DNA scaffold at key positions. For example, the polymerase subassemblies are bound to the leading- and lagging-strand primer–template DNA junctions, where they catalyze the individual steps of nucleotide addition. Similarly, the helicase–primase (primosome) subassembly is bound at the moving replication fork junction of the elongation–replication complex to catalyze the sequential unwinding steps of the genomic double-stranded DNA (dsDNA) ahead of the polymerases while synthesizing the pentameric RNA primers that are needed to reinitiate lagging-strand DNA synthesis at the ends of completed lagging-strand ssDNA (Okazaki) fragments. While exposed in single-stranded form the ssDNA templates are coated by cooperatively bound ssDNA-binding proteins that function to integrate the activities of the spatially separated replication subassemblies.

The nucleic acid framework shown in **Figure 1*b*** is the same as that in **Figure 1*a***, except the protein components have been removed to reveal the underlying ssDNA–dsDNA forks and primer–template junctions to which the individual protein subassemblies bind during the various processes of DNA replication, as well as during DNA recombination and repair and RNA transcription. Because the replication subassemblies must function independently of the local base sequence or composition of the DNA, their binding affinities and interactions with the DNA scaffold cannot be base sequence specific but must depend only on the local secondary structures of the bases, base pairs, and sugar-phosphate backbones at the various ssDNA–dsDNA binding site junctions. Thus, this system is well suited for study by exciton-coupled dimer probe spectroscopies that sense primarily local DNA backbone conformations.

1.2. Site-Specific Free Energy Landscape Descriptions of the Assembly of Protein–DNA Complexes

To obtain molecular level insights into the assembly and functional mechanisms of multicomponent complexes such as the T4 DNA replisome, one must identify key features of the underlying macromolecular interactions. A useful concept for this purpose is the free energy landscape, which describes variations in the stability of protein and nucleic acid components at a specific interaction site and as a function of relevant chemical reaction coordinates. In **Figure 2**, we present a

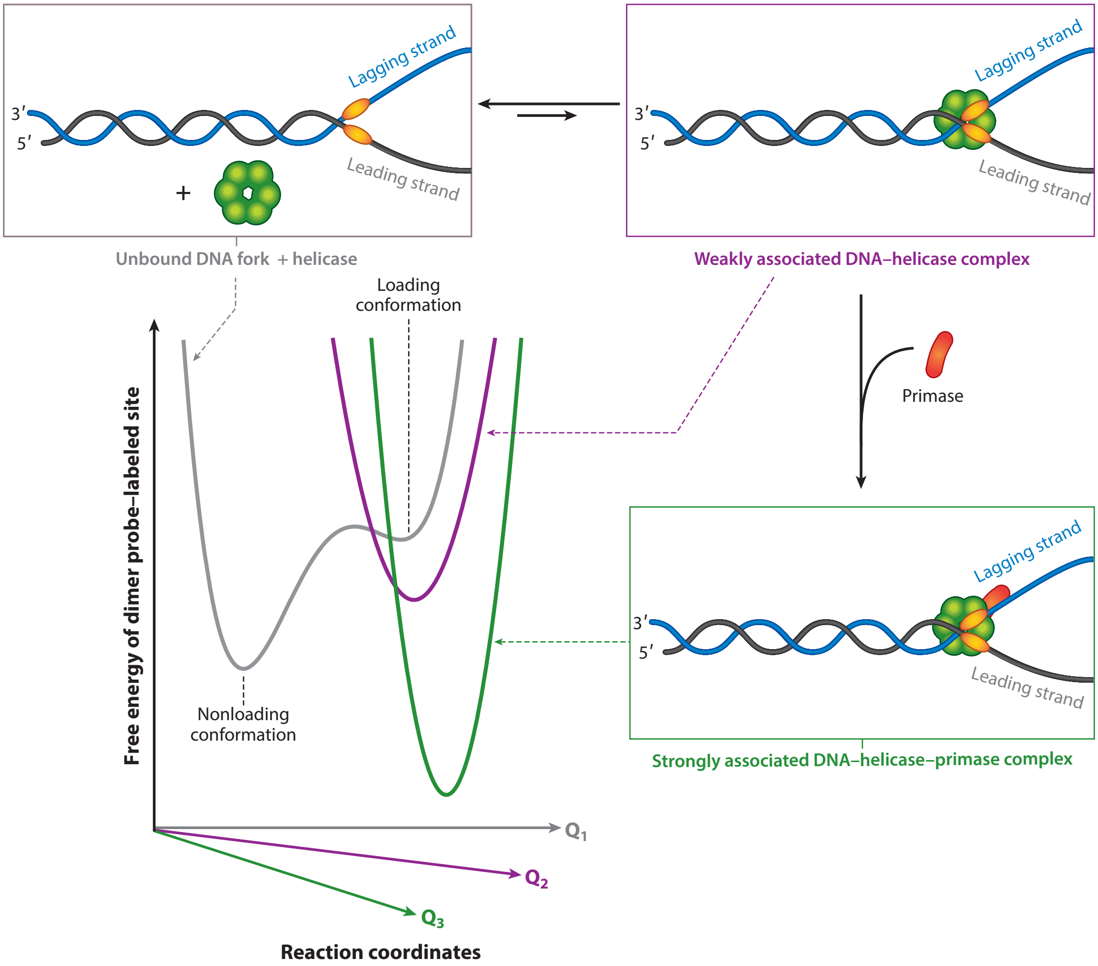

Figure 2

Hypothetical free energy surface for the successive assembly steps of the T4 helicase–primase (primosome)–DNA fork subassembly as monitored by $(\mathrm{iCy3})_2$ dimer backbone probes (indicated by *yellow ovals*). Successive reaction steps are indicated by gray, purple, and green 2D cross sections of the multidimensional free energy surface. Figure adapted from References 11, 12. Abbreviation: $(\mathrm{iCy3})_2$, internally labeled exciton-coupled cyanine.

hypothetical free energy surface for the cooperative assembly steps of the T4 helicase–primase–DNA fork complex. This picture illustrates the postulated role of DNA "breathing" at a specific site near the ssDNA–dsDNA fork junction where the helicase and primase must preferentially bind and assemble in a defined temporal sequence. In the absence of proteins, the sugar-phosphate backbones at a specific position near the ssDNA–dsDNA fork junction may fluctuate between a stable protein–nucleic acid conformation that does not favor functional helicase loading onto the replication fork and an unstable conformation that favors such loading. The association of a weakly bound helicase with the subsequent formation of a stable and fully functional helicase–primosome complex is represented as a series of successive surface crossing events.[2]

---

[2] Note that the cross-sectional components of the free energy landscape indicated in **Figure 2** are not to be confused with Born–Oppenheimer excited electronic potential energy surfaces between which relatively fast

The free energy landscape picture emphasizes the central role of local structural fluctuations (i.e., DNA breathing) of the ssDNA–dsDNA fork junction in the cooperative protein–DNA assembly process. In the example shown in **Figure 2**, we focus on the local fluctuations of the sugar-phosphate backbones at key sites relative to the ssDNA–dsDNA fork junction at which functional protein–DNA interactions occur that are essentially independent of DNA base sequence. In contrast, conformational fluctuations of the DNA bases (e.g., base stacking and unstacking) direct protein–DNA interactions involved in the recognition of specific DNA base sequences, such as the binding of a transcription factor to a promoter site, where initiation of the transcription of a specific gene occurs. Points on the free energy surface corresponding to free energy minima and maxima define the local conformations of stable macrostates and unstable transition states, respectively, that lie along the assembly pathway of a specific protein–DNA interaction process. Furthermore, the thermodynamic basins that surround each local minimum of the free energy surface are associated with distributions of quasi-degenerate conformations that define the conformational disorder of a given macrostate.

2. EXCITON-COUPLED DIMER PROBE SPECTROSCOPY

Although well-established structural tools such as nuclear magnetic resonance (NMR) and X-ray crystallography provide detailed molecular level information about stable protein–nucleic acid complexes at relatively high concentrations (13), such methods are not well suited to study site-specific protein–DNA interactions at the micromolar-to-nanomolar concentrations typical of protein–DNA complex assembly and function processes. An alternative approach, which can be applied at physiological concentrations, is to perform optical spectroscopic experiments on DNA constructs that have been site-specifically labeled with exciton-coupled dimer probes (14–16).

2.1. Site-Specific $(Cy3)_2$ Dimer–Labeled DNA Fork Constructs

Carbocyanine dyes are useful fluorescent markers for labeling biological macromolecules due to their relatively high absorption cross sections and fluorescence quantum yields (17). For example, measurements of Förster resonant energy transfer between the carbocyanine dyes Cy3 and Cy5 are often used to monitor structural changes of DNA on the length scale of a few nanometers (18). Cy3 can be attached at internal positions (iCy3) within the framework of a DNA strand by phosphoramidite chemistry (17, 19). Such an internal iCy3 label acts as a relatively stiff molecular bridge between DNA bases and as part of the sugar-phosphate backbone connecting adjacent nucleotide residues (see **Figure 3*a***).

By annealing two complementary single strands of DNA with opposite iCy3 labeling positions, one can form an exciton-coupled $(iCy3)_2$ dimer probe at a predetermined position within a model DNA duplex (**Figure 3*b***) or DNA fork construct (**Figure 3*c***). An annealed DNA fork construct contains both dsDNA and ssDNA regions, and the $(iCy3)_2$ dimer probe can be selectively inserted relative to the ssDNA–dsDNA fork junction (for probe-labeling nomenclature, see **Figure 3*d***). The spectroscopic properties of the $(iCy3)_2$ dimer depend sensitively on the relative orientation and spacing between the iCy3 monomers on the length scale of a few angstroms and thus can be used to determine the local conformations and conformational disorder of the sugar-phosphate backbones in model DNA constructs (14–16). iCy3 monomer–labeled DNA constructs can also be prepared by including a thymine (T) base in the complementary strand

---

(subnanosecond) nonadiabatic processes can occur. Rather, the surface crossing events depicted in **Figure 2** represent relatively slow (microseconds and longer) protein–nucleic acid interactions that occur exclusively in the ground electronic state.

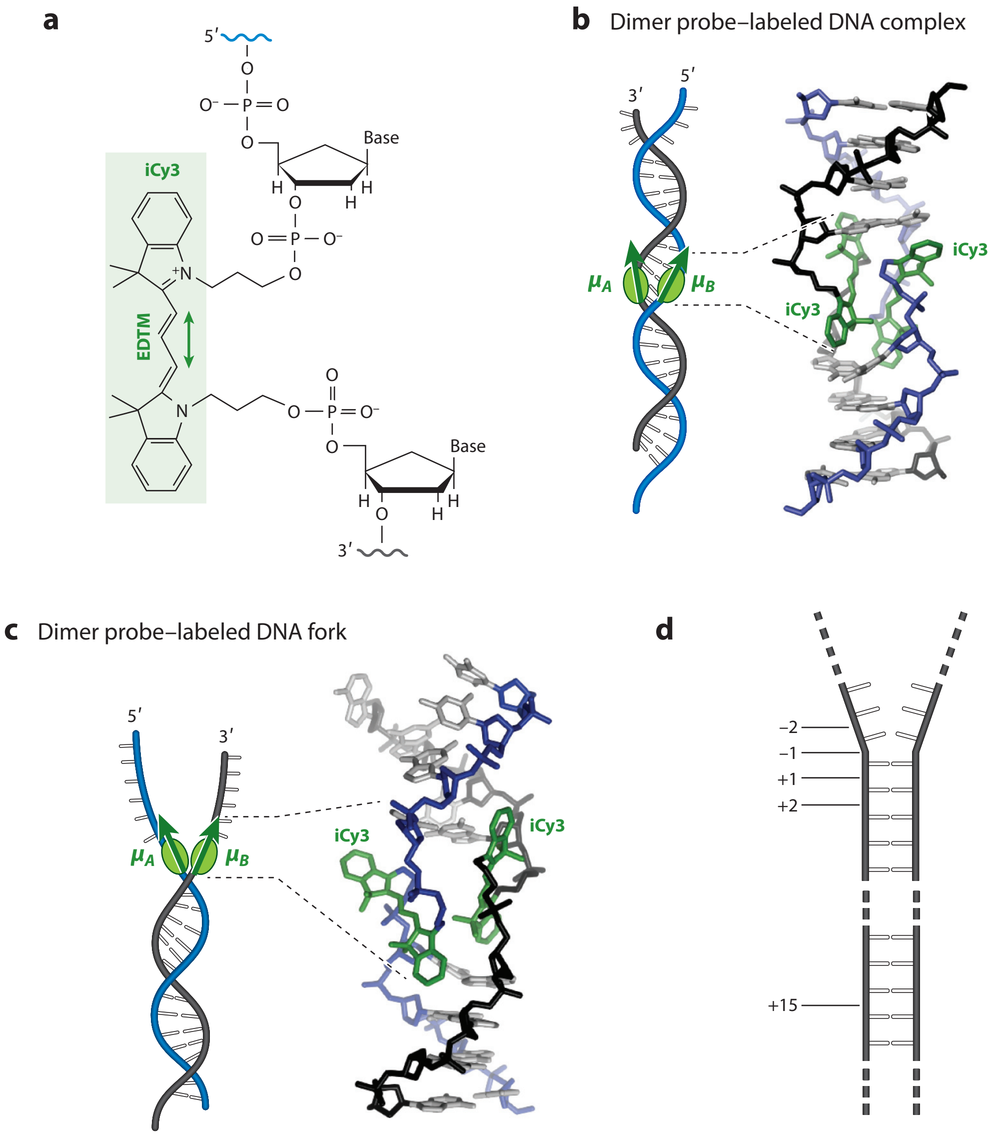

Figure 3

Labeling chemistry and nomenclature of the $(\text{iCy3})_2$ dimer probes positioned within the sugar-phosphate backbones of model ssDNA–dsDNA fork constructs. (*a*) The Lewis structure of the iCy3 chromophore is shown with its 3′ and 5′ linkages to the sugar-phosphate backbone of a local segment of ssDNA. The double-headed green arrow indicates the EDTM. (*b*) An $(\text{iCy3})_2$ dimer–labeled DNA duplex and (*c*) DNA fork construct contain the dimer probe at different positions relative to the ssDNA–dsDNA junction. (*d*) The insertion site position of the $(\text{iCy3})_2$ dimer probe is indicated relative to the fork junction using positive integers in the direction toward the double-stranded region and negative integers in the direction toward the single-stranded region. Figure adapted from References 14–16. Abbreviations: dsDNA, double-stranded DNA; EDTM, electric dipole transition moment; $(\text{iCy3})_2$, internally labeled exciton-coupled cyanine; ssDNA, single-stranded DNA.

at the position directly opposite the probe chromophore. The addition of the T base partially compensates for the misalignment of complementary base pairs introduced by the presence of the iCy3 monomer within one strand. $(\mathrm{iCy3})_2$ dimer–labeled DNA constructs exhibit relatively well-ordered, position-dependent local conformations that assume essentially the local conformational properties of the DNA duplex, especially when inserted into fully duplexed regions of a DNA scaffold such as that of the bacteriophage T4–coded DNA replisome (**Figure 1**).

2.2. Electronic-Vibrational (Vibronic) Model of the Cy3 Chromophore

The Cy3 chromophore consists of a conjugated trimethine bridge, which cojoins two indole-like substituents (as shown in **Figure 3*a***). The lowest-energy ($\pi \rightarrow \pi^*$) electronic transition between the ground and excited electronic states occurs in the visible region of the spectrum ($\lambda_{max} =$ 548 nm) when the molecule is in its all-*trans* ground state configuration (20). The transition energy of Cy3 is much lower than those of the component nucleotide residues of an unlabeled nucleic acid, and the electronic structure of the internally labeled iCy3 monomer is minimally affected by the surrounding macromolecular environment (14–16). The linear absorbance spectrum of free Cy3 in polar solvents, as well as when it is attached internally as iCy3 within a nucleic acid framework, is relatively insensitive to the local environment of the chromophore and exhibits a pronounced vibronic progression (**Figure 5*a***). Nevertheless, the vibronic spectrum of the iCy3 monomer plays a central role in determining the absorbance and circular dichroism (CD) spectra of such exciton-coupled $(\mathrm{iCy3})_2$ dimer–labeled ssDNA–dsDNA constructs, which are sensitive to the labeling position and local environment of the dimer probe (14–16).

Like many π-conjugated molecules, Cy3 exhibits numerous Franck–Condon active vibrational modes that range in energy from tens to several hundred wave numbers and that are vibronically coupled to the lowest-energy electronic transition (21–23). For the Cy3 chromophore in solution, thermal occupation of low-energy vibrational levels and rapid electronic dephasing lead to significant broadening of the vibronic fine structure. Furthermore, the single electronic transition is predominantly coupled to one low-frequency bending mode along the trimethine bridge, in combination with a cluster of relatively high-frequency modes in the vicinity of $\sim$1,100 cm^{-1} (23). The excited vibronic states of the Cy3 monomer in solution can be well approximated using a relatively simple quantum mechanical Hamiltonian $\hat{H}_M$ in which the $S_0 \rightarrow S_1$ transition (with energy $\varepsilon_0 = \sim 18{,}250\ \mathrm{cm}^{-1}$) is coupled to a single effective vibrational mode (with energy $\hbar\omega_{vib} = \sim 1{,}100\ \mathrm{cm}^{-1}$, see **Figure 4*a***) (14–16). The vibronic coupling is characterized by a Huang–Rhys parameter ($\lambda^2 = d^2\omega_{vib}/2\hbar = \sim 0.55$), which depends on the displacement (d) of the electronically excited vibrational potential energy surface relative to the ground state surface. The electric dipole transition moment (EDTM) is assumed to be independent of vibrational motion (the Condon approximation) and oriented parallel to the Cy3 trimethine bridge (**Figure 3*a***). In the absence of coupling to higher-lying electronic states, the single effective vibrational mode can be approximated as harmonic (21, 24). This simple vibronic state model for the iCy3 monomer in solution, although lacking in structural detail, has proven to be useful for characterizing the absorption spectrum of iCy3 monomer–labeled DNA duplex and fork constructs in which the probes are inserted at various positions and over a wide range of temperatures (14–16).

2.3. Holstein–Frenkel Model of $(\mathrm{iCy3})_2$ Dimer–Labeled DNA Constructs

Because the individual monomers within $(\mathrm{iCy3})_2$ dimer–labeled DNA constructs are separated by atomic scale distances, the monomer EDTMs (labeled $\boldsymbol{\mu}_A$ and $\boldsymbol{\mu}_B$ in **Figure 3**) can couple through a resonant electrostatic interaction J (25–27). The Holstein–Frenkel (H-F) Hamiltonian of the coupled dimer is written $\hat{H}_A + \hat{H}_B + J[|eg\rangle\langle ge| + |ge\rangle\langle eg|]$, where $|eg\rangle$ represents the product

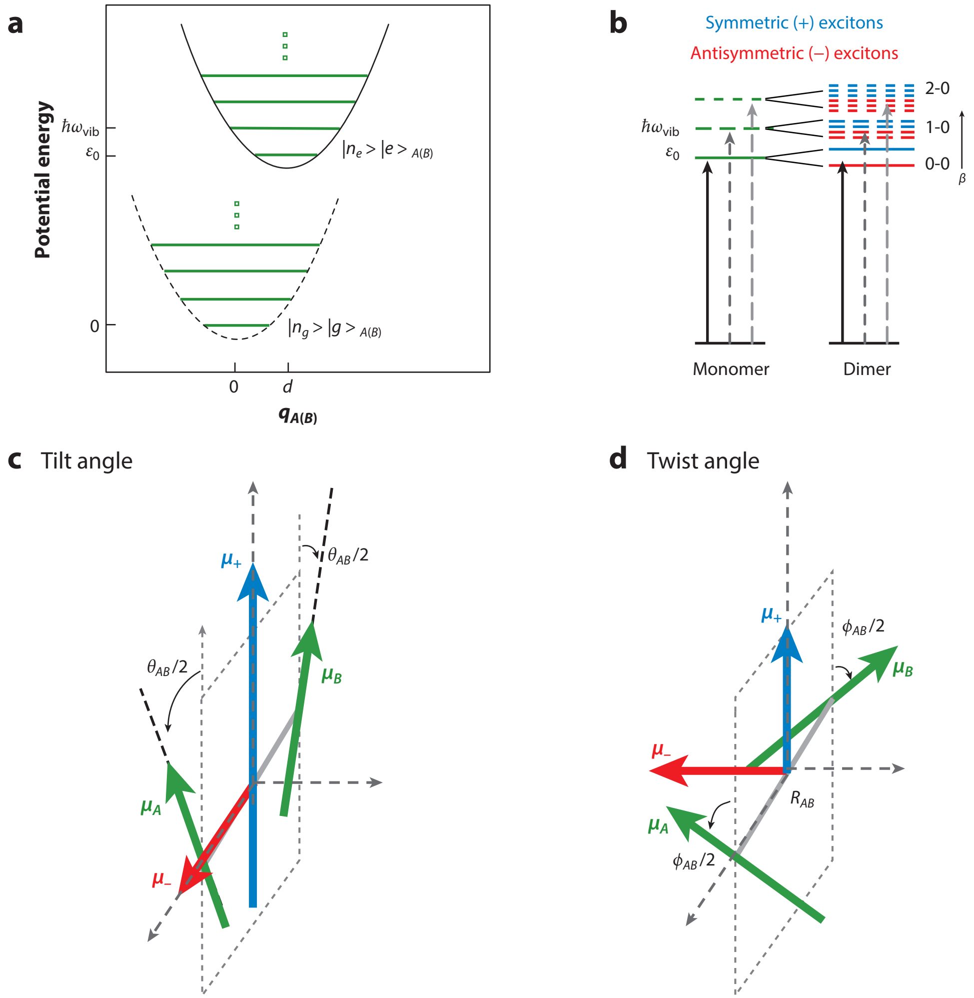

Figure 4

(*a*) Electronic-vibrational (vibronic) potential energy diagram for the iCy3 monomer [labeled $A(B)$] ground and excited electronic state levels, which are assumed to be coupled to a single effective high-frequency harmonic mode. (*b*) Electrostatic coupling J between the closely spaced monomers of the $(\mathrm{iCy3})_2$ dimer gives rise to delocalized symmetric (+, *blue*) and antisymmetric (−, *red*) excitons. The dimer structural parameters are (*c*) the tilt angle θ_{AB}, (*d*) the twist angle ϕ_{AB}, and the interchromophore separation R_{AB}. The electric dipole transition moments of the monomers are indicated by green arrows, and those of the symmetric (μ_+) and antisymmetric (μ_-) excitons are indicated by the blue and red arrows, respectively. Figure adapted from References 14–16. Abbreviation: $(\mathrm{iCy3})_2$, internally labeled exciton-coupled cyanine.

state in which monomer A is electronically excited and monomer B is unexcited. The electrostatic coupling gives rise to symmetric (+) and antisymmetric (−) Frenkel excitons with orthogonally polarized dipole moments $\boldsymbol{\mu}_\pm = \frac{1}{\sqrt{2}}[\boldsymbol{\mu}_A \pm \boldsymbol{\mu}_B]$ and with relative magnitudes that depend sensitively on the local conformation of the $(\mathrm{iCy3})_2$ dimer probe (see **Figure 4**). Each symmetric and antisymmetric exciton consists of a manifold of delocalized electronic-vibrationally coupled states, which are superpositions of electronic-vibrational products of the A and B monomer states, given by $|e_\pm^{(\beta)}\rangle = \sum_{n_e,n_g} c_\pm^{(\beta)}[u_{n_e,n_g}|eg\rangle \pm u_{n_g,n_e}|ge\rangle]$ (27). The coefficients $c_\pm^{(\beta)}$ depend on the vibrational coordinates of the monomers, where $u_{n_{e(g)},n_{g(e)}} = |n_{e(g)}n_{g(e)}\rangle$ is the vibrational product state, $n_{e(g)}$ is the vibrational quantum number in the electronic excited (ground) state, and $\beta = (0, 1, \ldots)$ is a state index in order of increasing energy (14–16) (see **Figure 4*b***).

The electrostatic coupling J depends on the dimer conformation and can be modeled in terms of the Coulomb interaction between the individual monomer transition charge densities. J can be approximated using models of varying levels of complexity. For example, the point-dipole (PD) approximation is often invoked to describe coupled molecular dimers, even for interchromophore separations smaller than the molecular dimension where the approximation is expected to be inaccurate (28). The PD approximation generally reflects the correct J-dependence on the monomer EDTM orientations while overestimating its overall magnitude. Improved estimates of J are obtained using the extended-dipole (ED) model, which accounts for the finite size of the Cy3 chromophores by approximating the transition charge density as a 1D line segment with partial charges concentrated at its end points (15, 24, 29). An atomistically detailed model, which is based on a 3D transition charge (TQ) density, assigns individual Mulliken transition charges to the atomic coordinates of the Cy3 chromophores (30, 31). In general, the value of J depends on the interchromophore tilt angle θ_{AB}, the twist angle ϕ_{AB}, and the separation R_{AB} (see **Figure 4*c*,*d***). When applied to the $(\text{iCy3})_2$ dimer, all three of the above models (PD, ED, and TQ) predict similar J-dependences on the orientational parameters, θ_{AB} and ϕ_{AB} (15).

2.4. Determining the Mean Local Conformations of $(\text{iCy3})_2$ Dimer–Labeled ssDNA–dsDNA Constructs by Linear Absorbance and Circular Dichroism Spectroscopy

Figure 5*a*,*b* demonstrates experimental room temperature (23°C) absorbance and CD spectra of iCy3 monomer– and $(\text{iCy3})_2$ dimer–labeled DNA constructs with probes inserted deep within the duplex region (+15 position), and an $(\text{iCy3})_2$ dimer–labeled DNA construct with probes inserted near the ssDNA–dsDNA junction (−1 position). As discussed in Section 2.2, the monomer absorbance spectrum is well approximated using a single effective mode Hamiltonian with lowest-lying optical transition centered at $\varepsilon_0 = {\sim}18{,}250\ \text{cm}^{-1}$ (the 0–0 line with no vibrational excitation) and sequentially higher-lying optical transitions (e.g., 1–0 and 2–0 with one and two vibrational excitations, respectively) spaced apart by the vibrational mode energy $\hbar\omega_{vib} = {\sim}1{,}100\ \text{cm}^{-1}$ (**Figure 5*a***). In this model, the peak intensities are given by the square modulus of the EDTM matrix elements $|\langle e|\langle n_e|\boldsymbol{\mu}_0|0\rangle|g\rangle|^2 = |\mu_0|^2|\langle n_e|0\rangle|^2$, where μ_0 (= ~12.8 D) is the magnitude of the iCy3 monomer EDTM, $|\langle n_e|0\rangle|^2 = e^{-\lambda^2}\lambda^{2n_e}/n_e!$ is the Franck–Condon factor, and λ^2 (= ~0.55) is the Huang–Rhys parameter (14–16). The CD signal is the differential absorbance between left- and right-handed circular polarized light, which is described by the Rosenfeld equation (32). Because CD depends on the presence of chiral asymmetry of the transition dipole moments, the (achiral) iCy3 monomer exhibits an approximately featureless CD spectrum (**Figure 5*b***). The absorbance and CD spectra of iCy3 monomer–labeled DNA constructs are largely insensitive to local environmental conditions, including temperature and insertion-site position relative to the ssDNA–dsDNA junction (14–16).

The vibronic progression seen in the iCy3 monomer–labeled DNA construct is also present in the absorbance spectra of the $(\text{iCy3})_2$ dimer–labeled duplex and fork DNA constructs. For the dimer systems, the strength of the electrostatic interaction lies within the so-called intermediate-coupling regime (33) so that the absorbance spectra of the dimer-labeled DNA constructs have qualitatively similar shapes to that of the monomer. However, the presence of electrostatic coupling leads to each of the vibronic features being split and additionally broadened into the symmetric (+) and antisymmetric (−) exciton subbands (see **Figure 4*b***).

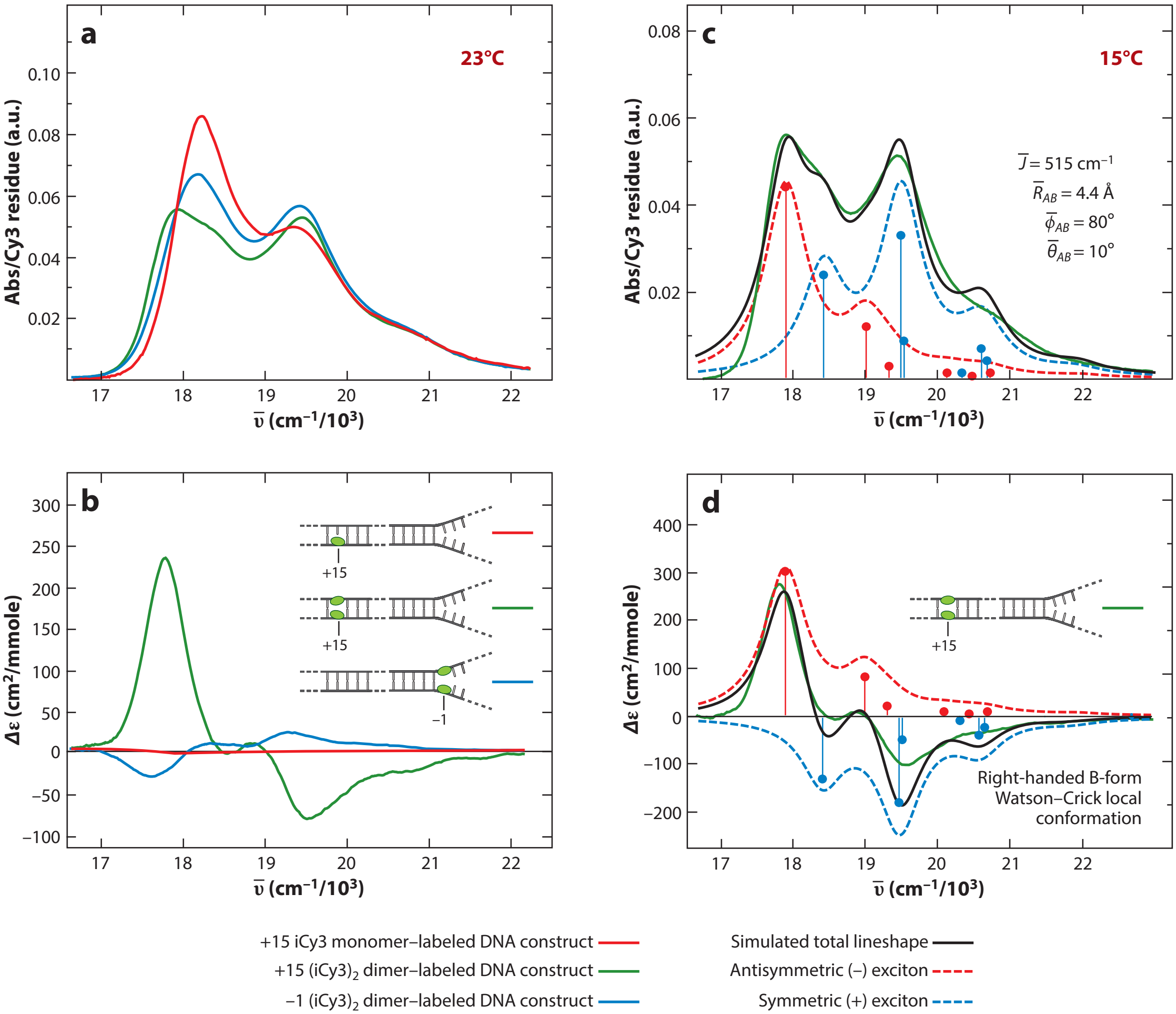

Figure 5

(*a*) Room temperature (23°C) experimental absorbance and (*b*) CD spectra for iCy3 monomer–labeled +15 duplex (*dashed red line*), (iCy3)$_2$ dimer–labeled +15 duplex (*green line*), and (iCy3)$_2$ dimer–labeled −1 fork (*blue line*) DNA constructs. (*c*) Experimental and simulated absorbance and (*d*) CD spectra for the (iCy3)$_2$ dimer–labeled +15 duplex DNA construct. Figure adapted from References 15, 16. Abbreviations: CD, circular dichroism; (iCy3)$_2$, internally labeled exciton-coupled cyanine.

The intensities of individual optical transitions of the (iCy3)$_2$ dimer–labeled DNA constructs (labeled by the energy index β) are given by the square modulus of the total EDTM matrix elements $|\langle 0|(\boldsymbol{\mu}_A + \boldsymbol{\mu}_B)|e_\pm^{(\beta)}\rangle|^2$. As can be seen from the absorbance spectra shown in **Figure 5*a***, the ratios of the 0–0 to 1–0 vibronic peak intensities for the dimers decrease relative to that of the monomer (i.e., $I_{0-0}^{dimer}/I_{1-0}^{dimer} < I_{0-0}^{mon}/I_{1-0}^{mon} = {\sim}1.60$) (14, 27). For an exciton-coupled dimer, the CD signal of individual optical transitions is proportional to the scalar triple product $\langle 0|\boldsymbol{\mu}_A|e_\pm^{(\beta)}\rangle \times \langle e_\pm^{(\beta)}|\boldsymbol{\mu}_B|0\rangle \cdot \boldsymbol{R}_{AB}$, where $\boldsymbol{R}_{AB}$ is the vector that joins the centers of monomers A and B (32) (see **Figure 4*d***). The triple product expression shows that the CD signal is zero for achiral conformations of the (iCy3)$_2$ dimer. Thus, the strong CD signals observed for the (iCy3)$_2$ dimer–labeled fork and duplex ssDNA–dsDNA constructs (**Figure 5*b***) indicate the presence of chiral dimer conformations at these probe-labeling sites. In both cases the CD spectra exhibit a progression of bisignate lineshapes (i.e., a change of sign within a given vibronic band), which is a feature of vibronic excitons in a chiral dimer (34). Moreover, the CD spectra of the two $(\mathrm{iCy3})_2$ dimer–labeled DNA constructs (+15 duplex versus −1 fork) have opposite signs, indicating that the two systems have opposite chiral symmetries.

As an example of the conformational analysis that is applied to $(\mathrm{iCy3})_2$ dimer–labeled ssDNA–dsDNA constructs, **Figure 5*c*,*d*** shows the absorbance and CD spectra of the $(\mathrm{iCy3})_2$ dimer–labeled +15 duplex DNA construct measured at 15°C. Overlaid with the experimental spectra are optimized model fits, which are based on the single effective mode H-F Hamiltonian using an ED approximation for the electrostatic coupling (15, 16). The symmetric and antisymmetric exciton components are plotted. The optimized values for the mean structural parameters are $\bar{J} = 515\ \mathrm{cm}^{-1}$, $\bar{R}_{AB} = 4.4$ Å, $\bar{\phi}_{AB} = 80°$, and $\bar{\theta}_{AB} = 10°$. These values are consistent with space-filling models for the local conformation of the $(\mathrm{iCy3})_2$ dimer depicted in **Figure 3*b***, which shows the two iCy3 monomers positioned closely within the DNA duplex with an approximately coplanar and nearly orthogonal relative orientation. This dimer conformation reflects the anticipated right-handed B-form (Watson–Crick) structure of the opposing segments of the sugar-phosphate backbones deep within the duplex region of the DNA construct.

In general, the agreement between experiment and theory using the H-F model for $(\mathrm{iCy3})_2$ dimer–labeled ssDNA–dsDNA constructs is very good over a broad range of experimental conditions, including varying temperature and probe-labeling position relative to the ssDNA–dsDNA junction (14–16). Both simulated absorbance and CD spectra reflect the experimentally observed effects of intensity-borrowing between the 0–0 and 1–0 subbands [i.e., the diminished oscillator strength of the lowest-energy (0–0) antisymmetric transition and the enhanced oscillator strength of the vibrationally excited (1–0) symmetric transition], which is a direct consequence of the electrostatic coupling (22, 24, 27). However, as seen in **Figure 5*c*,*d***, the theory generally fails to predict the exact spectral lineshapes, as it tends to overestimate the intensities of the blue-edge shoulder of the 0–0 feature and the vibrationally excited 1–0 and 2–0 features. This shortfall is due most likely to the inaccuracies of the vibronic Hamiltonian used to describe the iCy3 monomer, which assumes a single effective harmonic mode (23). Nevertheless, the H-F model provides an adequate description of experimental absorbance and CD spectra of the $(\mathrm{iCy3})_2$ dimer–labeled ssDNA–dsDNA constructs under systematically adjusted environmental conditions, which can be interpreted in terms of the mean structural parameters $\bar{J}$, $\bar{R}_{AB}$, $\bar{\phi}_{AB}$, and $\bar{\theta}_{AB}$.

2.5. Probing Local Conformational Distributions of $(\mathrm{iCy3})_2$ Dimer–Labeled ssDNA–dsDNA Constructs by 2D Fluorescence Spectroscopy

In addition to providing the mean local conformation of an $(\mathrm{iCy3})_2$ dimer–labeled DNA construct in solution, the theoretical lineshape analysis discussed in Section 2.4 accounts for the presence of conformational heterogeneity within the ensemble. For the fits shown in **Figure 5*c*,*d***, the homogeneous lineshapes of individual spectral features were assumed to be Lorentzian with full width at half maximum $\Gamma_H = 160\ \mathrm{cm}^{-1}$ (16). The total spectral lineshapes were simulated by performing a convolution integral (i.e., a so-called Voigt profile) of the homogeneous spectral features with an inhomogeneous distribution function (modeled as a normal Gaussian with standard deviation $\sigma_I = 137\ \mathrm{cm}^{-1}$). The width of the inhomogeneous distribution is a direct measure of conformational heterogeneity (or disorder) of the $(\mathrm{iCy3})_2$ dimer–labeled DNA construct, which can vary depending on temperature and probe-labeling position. The homogeneous line width is dominated by pure dephasing, which depends on direct interactions between the electronic transitions of the $(\mathrm{iCy3})_2$ dimer probes and the phonon bath of their local environments that is composed primarily of the sugar-phosphate backbones. As such, the values of both the homogeneous and the inhomogeneous line width parameters, Γ_H and σ_I, respectively, are sensitive to opposing aspects of local structure; Γ_H is proportional to the presence of local order and σ_I is proportional to the degree of conformational heterogeneity.

For our structural analyses of $(\text{iCy3})_2$ dimer–labeled ssDNA–dsDNA constructs, the mean conformational parameters (i.e., $\bar{J}$, $\bar{R}_{AB}$, $\bar{\phi}_{AB}$, and $\bar{\theta}_{AB}$) were determined from linear absorbance and CD spectra, and information about the spectral line width parameters related to conformational heterogeneity was obtained by performing independent nonlinear 2D fluorescence spectroscopy (2DFS) experiments. 2DFS is a fluorescence-detected Fourier transform (FT) optical spectroscopy whose underlying principles resemble those of 2D NMR (35, 36) and is closely related to transmission-detected FT optical spectroscopies in the visible and IR regimes (37–39). Highly sensitive fluorescence-detected FT spectroscopies, and related action signal–based FT methods (40–50), have been reviewed in recent years (51, 52). The technical details of the 2DFS instrument used in our cyanine dimer experiments are reported in the source material (14–16, 42).

In 2DFS, a repeating sequence of four collinear optical pulses is generated using interferometric methods (**Figure 6*a***). The laser is optically resonant with the symmetric and antisymmetric excitons of the $(\text{iCy3})_2$ dimer–labeled ssDNA–dsDNA constructs, such that each of the four pulses can excite a one-photon dipole-allowed transition between ground, singly excited and doubly excited states. The resulting fluorescence signal is proportional to the nonlinear populations of molecular excited states. The recorded signals are t_{21}-, t_{43}-dependent oscillatory response functions (the waiting time t_{32} is set to zero) that depend on the relative pulse phases, φ_{21} and φ_{43}, which are continuously swept at radio frequencies. FT with respect to t_{21} and t_{43} yields the frequency-dependent nonrephasing (NRP) and rephasing (RP) 2D spectra. Example experimental 2D spectra are shown in **Figure 6*b*** for the +15 duplex $(\text{iCy3})_2$ dimer–labeled ssDNA–dsDNA construct taken at 15°C and under physiological buffer salt conditions (16). The 2D spectra exhibit diagonal peaks and off-diagonal cross-peaks corresponding to the 0–0 and 1–0 vibronic transitions.

An important feature of the RP and NRP response functions is their distinct dependences on the values of Γ_H and σ_I. When the effects of inhomogeneous broadening are included (16, 47, 53), the RP response function contains the lineshape factor $\exp[-\Gamma_H(t_{21}+t_{43})]\exp[-\sigma_I^2(t_{21}-t_{43})^2/2]$, which decays exponentially along the collective coordinate $(t_{21}+t_{43})$ and as a Gaussian envelope with inhomogeneous decay constant $\sigma_I^2/2$ along the relative coordinate $(t_{21}-t_{43})$. In contrast, the NRP response function contains the lineshape factor $\exp[-\Gamma_H(t_{21}+t_{43})]\exp[-\sigma_I^2(t_{21}+t_{43})^2/2]$, which decays along the collective coordinate with rate constants that depend on both Γ_H and σ_I. In our analyses of the 2D spectral lineshapes of iCy3 monomer and $(\text{iCy3})_2$ dimer ssDNA–dsDNA constructs, we determined Γ_H and σ_I by simultaneously fitting experimental RP and NRP 2DFS data to the numerical FTs of the model response functions (16). This approach provides an accurate description of the 2D spectra without imposing any assumed restrictions on the degree of inhomogeneity present.

2.6. Position- and Temperature-Dependent Local Conformational Distributions of $(\text{iCy3})_2$ Dimer–Labeled ssDNA–dsDNA Constructs

We carried out room temperature absorbance, CD, and 2DFS experiments on +2, +1, −1, and −2 $(\text{iCy3})_2$ dimer–labeled ssDNA–dsDNA constructs in which the position of the dimer probe was systematically varied across the ssDNA–dsDNA junction (15, 16). The results of these studies show that the mean electrostatic coupling $\bar{J}$ undergoes a sign inversion as the $(\text{iCy3})_2$ dimer probe position is changed from the +1 to the −1 position of the ssDNA–dsDNA construct, indicating

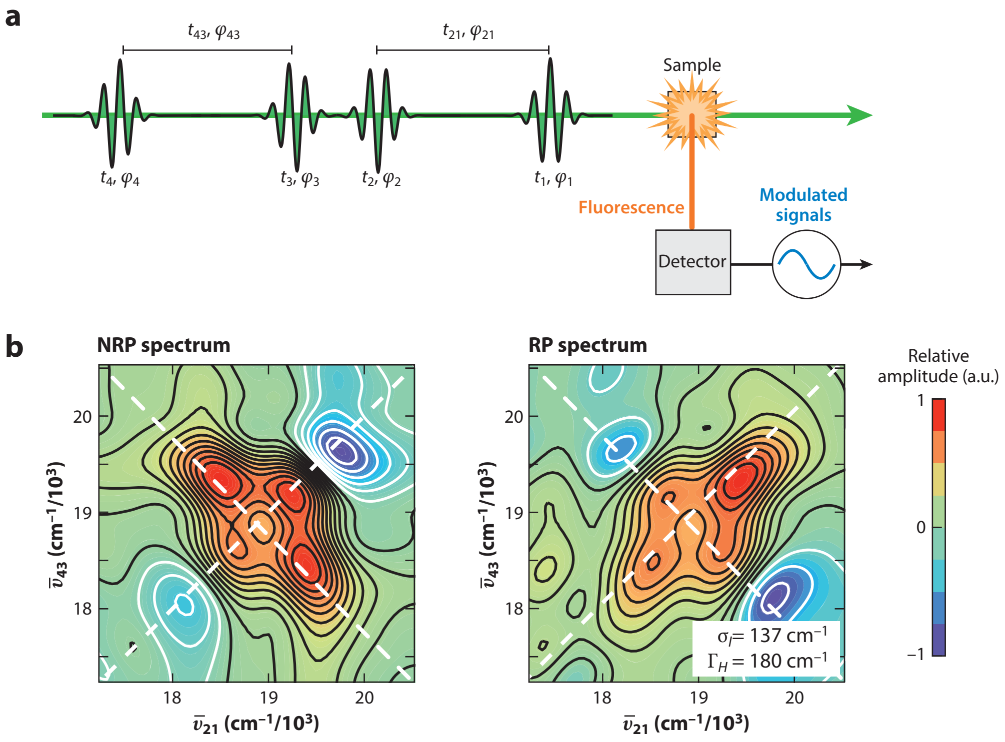

Figure 6

(*a*) The 2DFS instrument prepares a train of four collinear optical pulses with relative phases, $\varphi_{21}, \varphi_{43}$, and time delays, t_{21}, t_{43}. The ensuing fluorescence is detected as a function of the pulse delays and phases. (*b*) Real parts of experimental NRP and RP 2D fluorescence spectra of the +15 duplex (iCy3)$_2$ dimer–labeled ssDNA–dsDNA construct. The optimized values of Γ_H and σ_I are shown in the inset. Figure adapted with permission from Reference 16. Abbreviations: 2DFS, 2D fluorescence spectroscopy; dsDNA, double-stranded DNA; (iCy3)$_2$, internally labeled exciton-coupled cyanine; NRP, nonrephasing; RP, rephasing; ssDNA, single-stranded DNA.

that the conformation of the (iCy3)$_2$ dimer probe, and presumably that of the sugar-phosphate backbones labeled at these sites, changes from right-handed to left-handed. This change of handedness is correlated to a change in the mean twist angle $\bar{\phi}_{AB}$ from a value that is less than 90° (right-handed) to a value that is greater than 90° (left-handed). In addition, the mean tilt angle $\bar{\theta}_{AB}$ undergoes an abrupt increase between the +2 and the +1 positions, followed by a decrease at the −1 and −2 positions. Thus, local conformations of the sugar-phosphate backbones undergo an abrupt loss of cylindrical symmetry at the interface between the +2 and the +1 positions, which is partially recovered at the −1 and −2 positions.

Analyses of 2DFS measurements show how the local conformational heterogeneity of the (iCy3)$_2$ dimer probe depends on the labeling position (16). These studies reveal that there is a higher degree of conformational heterogeneity at the +2 position relative to the +15 position. When the probe-labeling position is changed from +2 to +1, the conformational heterogeneity increases significantly, suggesting that the distribution of local conformations is further broadened. However, the conformational heterogeneity at the +1 position is maximal. When the probe-labeling position is changed to −1, and then again to −2, the conformational heterogeneity decreases slightly relative to +1.

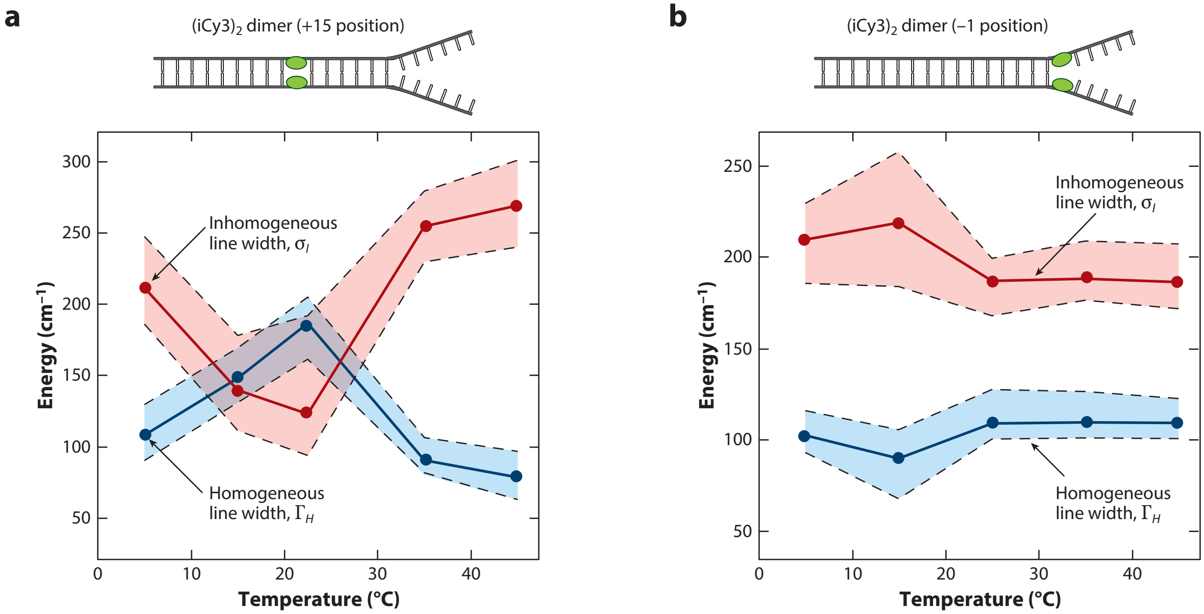

Figure 7

Optimized homogeneous and inhomogeneous line width parameters as a function of temperature obtained from 2D fluorescence spectroscopy lineshape analyses. Experiments were carried out under physiological salt conditions. (*a*) (iCy3)$_2$ dimer–labeled +15 ssDNA–dsDNA construct, and (*b*) (iCy3)$_2$ dimer–labeled −1 ssDNA–dsDNA construct. The temperature- and position-dependent behavior of Γ_H and σ_I are shown as light blue– and coral-shaded regions, respectively. The optimized values are presented as points, and the shaded regions bounded by dashed lines indicate error bars. Figure adapted with permission from Reference 16. Abbreviations: dsDNA, double-stranded DNA; (iCy3)$_2$, internally labeled exciton-coupled cyanine; ssDNA, single-stranded DNA.

We further examined how conformational heterogeneity of the (iCy3)$_2$ dimer probe depends on temperature by performing 2DFS experiments on the +15 duplex and −1 fork constructs (16). **Figure 7** shows the results of these studies, which provide a detailed picture of the temperature- and position-dependent behavior of Γ_H and σ_I.

We find that at room temperature and physiological buffer salt conditions, the local conformation of the (iCy3)$_2$ dimer probes at the +15 position is minimally disordered, such that the probes interact uniformly with their local environments to maximize the electronic dephasing rate. The room temperature condition appears to be unique. As the temperature is raised or lowered from 23°C, the local conformational heterogeneity increases abruptly, while the mean coupling strength between electronic transitions of the probe chromophores and the phonon bath decreases. We thus find that the Watson–Crick (B-form) local conformation of the (iCy3)$_2$ dimer–labeled sugar-phosphate backbones at sites deep within the duplex region is an optimally stable structure at 23°C, and that the distribution of conformations broadens substantially at temperatures just above or below room temperature. These findings are consistent with the notions that the room temperature stability of the local B-form conformation results from a nearly equal balance between opposing thermodynamic forces (entropy-enthalpy compensation) and that small departures from room temperature (in either the positive or negative directions) alter the free energy landscape and populate non-B-form conformations. Such a picture is sometimes invoked in DNA breathing and trapping models, in which noncanonical local conformations of the DNA framework are transiently populated under physiological conditions and function as activated states required for protein–DNA complex assembly (11, 12, 54, 55).

For the $(\mathrm{iCy3})_2$ dimer–labeled ssDNA–dsDNA −1 fork construct, in which the mean local conformation of the sugar-phosphate backbones at room temperature is left-handed and relatively disordered (compared with the +15 position), increasing the temperature above 23°C does not significantly change the local conformational heterogeneity (**Figure 7*b***). However, like our observation for the +15 duplex ssDNA–dsDNA construct, decreasing temperature below 23°C leads to a significant increase of conformational heterogeneity at the −1 position.

3. CONCLUSIONS

The conservation of base sequence integrity within genomic DNA is critical to maintaining well-regulated gene expression and replication. However, the structure of DNA within the cell must be dynamic, allowing for thermally induced fluctuations (i.e., DNA breathing) to facilitate productive interactions, including binding site recognition and the assembly of functional protein–DNA complexes. For example, at ssDNA–dsDNA fork junctions, transient local conformational fluctuations of the sugar-phosphate backbones are likely transition states for the formation of a stable helicase–primase (primosome) subassembly during DNA replication, with the existence of multiple DNA conformers working to facilitate competition between different protein regulatory factors and replisome proteins (**Figure 2**).

Our observations for both the fork and the duplex ssDNA–dsDNA constructs suggest, as has been studied in protein systems, that the concept of cold denaturation (defined as points in the phase diagram for the folding–unfolding transition of the protein in which changes in temperature in either direction decrease the stability of the folded form) might be productively applied to investigate the stability of ssDNA–dsDNA constructs as well (56–59). Future studies of nucleic acid stability, using the 2DFS approach to investigate conformational disorder at nucleic acid positions of possible physiological interest, may help to reveal new insights into the underlying molecular mechanisms of processes central to genome expression.

Figure 8 summarizes the results of our position-dependent studies of the $(\mathrm{iCy3})_2$ dimer–labeled ssDNA–dsDNA constructs at room temperature (16), which provide a detailed picture of the mean local conformations and conformational heterogeneity of the sugar-phosphate backbones at positions across the ssDNA–dsDNA fork junction. For positive integer positions the mean local conformation of the sugar-phosphate backbones is right-handed, and for negative integer positions the mean local conformation is left-handed. Local conformations deep within the duplex region are cylindrically symmetric and minimally disordered. The disorder increases significantly for positive positions approaching the ssDNA–dsDNA fork junction. At the +1 position, there is an abrupt loss of cylindrical symmetry, which coincides with an additional increase in conformational disorder. The left-handed conformations at the −1 and −2 positions exhibit somewhat smaller mean tilt angles and decreasing conformational disorder, suggesting that the peak perturbation to secondary structure within the ssDNA–dsDNA fork junction occurs at the +1 position.

Our 2DFS experiments provide additional information about the standard deviations of the distributions of conformational coordinates (16). It is perhaps surprising that our results indicate that the distributions of conformational parameters at positions traversing the ssDNA–dsDNA fork junction are narrow, suggesting that regions of the junction extending toward and into the single-stranded segments of the overall junction are relatively well ordered. A possible explanation is that the sugar-phosphate backbones can adopt only a small number of local conformations whose relative stabilities depend on their positions within the junction. This concept is illustrated in **Figure 8*b*** using hypothetical free energy surfaces, each of which depicts four possible local conformations of the sugar-phosphate backbones, with the right-handed Watson–Crick

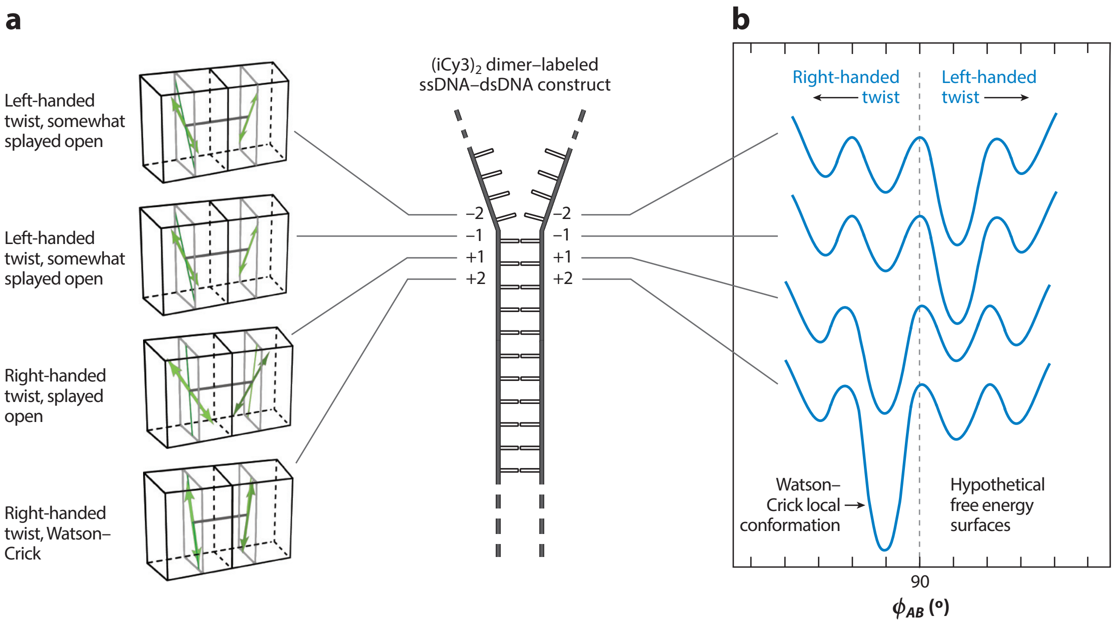

Figure 8

(*a*) Schematic of the position-dependent changes in mean local conformations of the $(iCy3)_2$ dimer–labeled ssDNA–dsDNA construct. (*b*) Hypothetical free energy landscape specific to the probe-labeling position. Individual surfaces are vertically offset for clarity. Figure adapted with permission from Reference 16. Abbreviations: dsDNA, double-stranded DNA; $(iCy3)_2$, internally labeled exciton-coupled cyanine; ssDNA, single-stranded DNA.

(B-form) conformation being the most favored at positive integer positions. In this picture the free energy differences between the Watson–Crick ground state and the other (noncanonical) local conformations are sufficiently high to ensure that the Boltzmann-weighted distributions of available macrostates are dominated by the Watson–Crick structure. At the same time, the moderate free energies of activation allow for infrequent transitions between noncanonical local structures, which are present in trace amounts. As the probe-labeling position is moved across the ssDNA–dsDNA junction toward the single-stranded regions, the free energy surfaces exhibit local minima with approximately the same coordinate values but with the most favored (ground state) conformation shifted to reflect the left-handed structures observed in our experiments (15, 16). Studies currently underway in our laboratories are designed to show how the free energy surfaces corresponding to critical positions within the DNA framework of the T4 replisome (**Figure 1*b***) are shifted relative to one another and are modulated in the presence of proteins that operate at these sites in regulating the function of the entire complex (**Figure 1*a***).

4. OUTLOOK

In this review, we have focused on the application of ensemble spectroscopic measurements (i.e., absorbance, CD, and 2DFS) to study the local conformations and conformational heterogeneity of ssDNA–dsDNA fork junctions viewed primarily through the lens of exciton-coupled $(iCy3)_2$ dimer probe labels of the sugar-phosphate backbones. These methods provide detailed molecular level information about the average local conformations and conformational distributions associated with the stable macrostates that exist for a given protein–DNA complex. The systems described in the current review can be further studied using single-molecule fluorescence measurements (12, 54, 60, 61) to directly probe the conformational fluctuations of the sugar-phosphate backbones of ssDNA–dsDNA constructs over timescales ranging from microseconds to hundreds of milliseconds. In principle, such single-molecule kinetic experiments can provide detailed mechanistic information about the rates of interconversion between stable macrostates, the identities and roles of metastable reactive intermediates, and the connected pathways of protein–DNA complex assembly processes. Additional information about the local conformations and conformational disorder of the DNA bases can be obtained spectroscopically using DNA constructs in which one or more bases has been site-specifically substituted with a fluorescent base analogue (62–65). The relatively unfavorable spectroscopic properties of fluorescent base-analogue-substituted DNA constructs (e.g., low-fluorescence quantum yields, low-absorption cross sections, inefficient photodetection at near-UV wavelengths) have been an obstacle for carrying out studies similar to those discussed in this review for cyanine probes. Nevertheless, recent developments in phase-sensitive photon-counting detection (50) and low-flux two-photon FT interferometry (49, 66–69) suggest that a new chapter in quantitative spectroscopic analysis of UV-absorbing molecular probes is currently on the horizon.

DISCLOSURE STATEMENT

The authors are not aware of any affiliations, memberships, funding, or financial holdings that might be perceived as affecting the objectivity of this review.

ACKNOWLEDGMENTS

The authors are grateful to former members of the Marcus and von Hippel groups for their contributions. A.H.M. would like to acknowledge helpful discussions with Spiridoula Matsika and Marina Guenza. This work was supported by grants from the National Institutes of Health General Medical Sciences (grant GM-15792 to A.H.M. and P.H.v.H.) and the National Science Foundation Chemistry of Life Processes Program (grant CHE-1608915 to A.H.M.). P.H.v.H. is an American Cancer Society Research Professor of Chemistry.

LITERATURE CITED

1. Alberts B, Johnson A, Lewis J, Raff M, Roberts K, Walter P. 2008. *Molecular Biology of the Cell*. New York: Garland Science
2. Kuriyan J, Konfuri B, Wemmer D. 2013. *The Molecules of Life*. New York: Garland Science
3. Phillips R, Kondev J, Theriot J, Garcia H. 2012. *Physical Biology of the Cell*. New York: Garland Science
4. Benkovic SJ, Spiering MM. 2017. Understanding DNA replication by the bacteriophage T4 replisome. *J. Biol. Chem.* 292:18434–42
5. Lee W, Gillies JP, Jose D, von Hippel PH, Marcus AH. 2016. Single-molecule FRET studies of cooperative and non-cooperative binding kinetics of the bacteriophage T4 single-stranded DNA binding protein (gp32) to ssDNA lattices at replication fork junctions. *Nucleic Acids Res*. 44:10691–710
6. Alberts BM. 1987. Prokaryotic DNA replication mechanisms. *Philos. Trans. R. Soc. B* 317:395–420
7. Barry J, Wong ML, Alberts B. 2018. In vitro reconstitution of DNA replication initiated by genetic recombination: a T4 bacteriophage model for a type of DNA synthesis important for all cells. *Mol. Biol. Cell* 30:146–59
8. Sakabe K, Okazaki RA. 1966. A unique property of the replicating region of chromosomal DNA. *Biochim. Biophys. Acta Nucl. Acids Protein Synth.* 129:651–54
9. Kozlov AG, Shinn MK, Lohman TM. 2019. Regulation of nearest-neighbor cooperative binding of *E. coli* SSB protein to DNA. *Biophys. J.* 117:2120–40
10. von Hippel PH, Marcus AH. 2019. The many roles of binding cooperativity in the control of DNA replication. *Biophys. J.* 117:2143–46

11. von Hippel PH, Johnson NP, Marcus AH. 2013. 50 years of DNA 'breathing': reflections on old and new approaches. *Biopolymers* 99:923–54
12. Phelps C, Lee W, Jose D, von Hippel PH, Marcus AH. 2013. Single-molecule FRET and linear dichroism studies of DNA 'breathing' and helicase binding at replication fork junctions. *PNAS* 110:17320–25
13. Jordan SR, Pabo CO. 1988. Structure of lambda complex at 2.5 Å resolution: details of the repressor-operator interactions. *Science* 242:893–99
14. Kringle L, Sawaya N, Widom JR, Adams C, Raymer MG, et al. 2018. Temperature-dependent conformations of exciton-coupled Cy3 dimers in double-stranded DNA. *J. Chem. Phys.* 148:085101
15. Heussman D, Kittell J, Kringle L, Tamimi A, von Hippel PH, Marcus AH. 2019. Measuring local conformations and conformational disorder of $(Cy3)_2$ dimers labeled DNA fork junctions using absorbance, circular dichroism and two-dimensional fluorescence spectroscopy. *Faraday Disc.* 216:211–35
16. Heussman D, Kittell J, von Hippel PH, Marcus AH. 2022. Temperature-dependent local conformations and conformational distributions of cyanine dimer labeled single-stranded–double-stranded DNA junctions by 2D fluorescence spectroscopy. *J. Chem. Phys.* 156:045101-1-23
17. Levitus M, Ranjit S. 2011. Cyanine dyes in biophysical research: the photophysics of polymethine fluorescent dyes in biomolecular environments. *Q. Rev. Biophys.* 44:123–51
18. Murphy MC, Rasnik I, Cheng W, Lohman TM, Ha T. 2004. Probing single-stranded DNA conformational flexibility using fluorescence spectroscopy. *Biophys. J.* 86:2530–37
19. Lee W, von Hippel PH, Marcus AH. 2014. Internally labeled Cy3/Cy5 DNA constructs show greatly enhanced photostability in single-molecule FRET experiments. *Nucleic Acids Res.* 42:5967–77
20. Jia K, Wan Y, Xia A, Li S, Gong F, Yang G. 2007. Characterization of photoinduced isomerization and intersystem crossing of the cyanine dye Cy3. *J. Phys. Chem. A* 111:1593–97
21. Fulton RL, Gouterman M. 1961. Vibronic coupling. I. Mathematical treatment for two electronic states. *J. Chem. Phys.* 35:1059–71
22. Zhao Z, Spano FC. 2007. Multiple mode exciton-phonon coupling: applications to photoluminescence in oligothiophene thin films. *Phys J. Chem. C* 111:6113–23
23. Sorour M, Marcus AH, Matsika S. 2022. Modeling the electronic absorption spectra of the indocarbocyanine Cy3. *Molecules* 27(13):4062
24. Hestand NJ, Spano FC. 2018. Expanded theory of H- and J-molecular aggregates: the effects of vibronic coupling and intermolecular charge transfer. *Chem. Rev.* 118:7069–163
25. Fulton RL, Gouterman M. 1964. Vibronic coupling. II. Spectra of dimers. *J. Chem. Phys.* 41:2280–86
26. Eisfeld A, Braun L, Stunz WT, Briggs JS, Engel V. 2005. Vibronic energies and spectra of molecular dimers. *J. Chem. Phys.* 122:134103-1-10
27. Kistler KA, Pochas CM, Yamagata H, Matsika S, Spano FC. 2011. Absorption, circular dichroism, and photoluminescence in perylene diimide bichromophores: polarization-dependent H- and J-aggregate behavior. *J. Phys. Chem. B* 116:77–86
28. Howard IA, Zutterman F, Deroover G, Lamoen D, Van Alsenoy C. 2004. Approaches to calculation of exciton interaction energies for a molecular dimer. *J. Phys. Chem. B* 108:19155–62
29. Czikklely VHDF, Kuhn H. 1970. Extended dipole model for aggregates of dye molecules. *Chem. Phys. Lett.* 6:207–10
30. Kistler KA, Spano FC, Matsika S. 2013. A benchmark of excitonic couplings derived from atomic transition charges. *J. Phys. Chem. B* 117:2032–44
31. Sorour MI, Kistler KA, Marcus AH, Matsika S. 2021. Accurate modeling of exciton coupling in cyanine dye Cy3. *J. Phys. Chem. A* 125:7852–66
32. Nordén B, Rodger A, Dafforn T. 2010. *Linear Dichroism and Circular Dichroism: A Textbook on Polarized-Light Spectroscopy*. Cambridge, UK: RSC Publ.
33. Förster T. 1965. *Delocalized excitation and excitation transfer*. Bull. 18., Div. Biol. Med., U.S. Atomic Energy Comm., Fla. State Univ., Tallahassee
34. Harada N, Berova N. 2012. Spectroscopic analysis: exciton circular dichroism for chiral analysis. In *Comprehensive Chirality*, ed. EM Carreira, H Yamamoto, pp. 449–77. Amsterdam: Elsevier
35. Mukamel S, Abramavicius D, Yang L, Zhuang W, Schweigert IV, Voronine DV. 2009. Coherent multidimensional optical probes for electron correlations and exciton dynamics: from NMR to X-rays. *Acc. Chem. Res.* 42:553–62

36. Jonas DM. 2003. Optical analogs of 2D NMR. *Science* 300:1515–17
37. Reppert M, Tokmakoff A. 2016. Computational amide I 2D IR spectroscopy as a probe of protein structure and dynamics. *Annu. Rev. Phys. Chem.* 67:359–86
38. Ghosh A, Ostrander JS, Zanni MT. 2017. Watching proteins wiggle: mapping structures with two-dimensional infrared spectroscopy. *Chem. Rev.* 117:10726–59
39. Laage D, Elsaesser T, Hynes JT. 2017. Water dynamics in the hydration shells of biomolecules. *Chem. Rev.* 117:10694–725
40. Tian P, Keusters D, Suzaki Y, Warren WS. 2003. Femtosecond phase-coherent two-dimensional spectroscopy. *Science* 300:1553–55
41. Tekavec PF, Dyke TR, Marcus AH. 2006. Wave packet interferometry and quantum state reconstruction by acousto-optic phase modulation. *J. Chem. Phys.* 125:194303-1-19
42. Tekavec PF, Lott GA, Marcus AH. 2007. Fluorescence-detected two-dimensional electronic coherence spectroscopy by acousto-optic phase modulation. *J. Chem. Phys.* 127:214307
43. Nardin G, Autry TM, Silverman KL, Cundiff ST. 2013. Multidimensional coherent photocurrent spectroscopy of a semiconductor nanostructure. *Opt. Express* 21:28617–27
44. Karki KJ, Widom JR, Seibt J, Moody I, Lonergan MC, et al. 2014. Coherent two-dimensional photocurrent spectroscopy in a PbS quantum dot photocell. *Nat. Commun.* 5:5869-1-7
45. De AK, Monahan D, Dawlaty JM, Fleming GR. 2014. Two-dimensional fluorescence-detected coherent spectroscopy with absolute phasing by confocal imaging of a dynamic grating and 27-step phase-cycling. *J. Chem. Phys.* 140:194201
46. Bruder L, Mudrich M, Stienkemeier F. 2015. Phase-modulated electronic wave packet interferometry reveals high resolution spectra of free Rb atoms and Rb*He molecules. *Phys. Chem. Chem. Phys.* 17:23877–85
47. Grégoire P, Kandada ARS, Vella E, Tao C, Leonelli R, Silva C. 2017. Incoherent population mixing of contributions to phase-modulated two-dimensional coherent excitation spectra. *J. Chem. Phys.* 147:114201
48. Tiwari V, Matutes YA, Konar A, Yu Z, Ptaszek M, et al. 2018. Strongly coupled bacteriochlorin dyad studied using phase-modulated fluorescence-detected two-dimensional electronic spectroscopy. *Opt. Express* 28:22327–41
49. Lavoie JTL, Smith B, Marcus AH, Raymer MG. 2020. Phase-modulated interferometry, spectroscopy and refractometry using entangled photon-pairs. *Adv. Quantum Tech.* 3:1900114
50. Tamimi A, Landes T, Lavoie J, Raymer MG, Marcus AH. 2020. Fluorescence-detected Fourier transform electronic spectroscopy by phase-tagged photon counting. *Opt. Express* 28:25194–214
51. Fuller FD, Ogilvie JP. 2015. Experimental implementations of two-dimensional Fourier transform electronic spectroscopy. *Annu. Rev. Phys. Chem.* 66:667–90
52. Tiwari V. 2021. Multidimensional electronic spectroscopy in high-definition—combining spectral, temporal, and spatial resolutions. *J. Chem. Phys.* 154:230901-1-17
53. Siemens ME, Moody G, Li H, Bristow AD, Cundiff ST. 2010. Resonance lineshapes in two-dimensional Fourier transform spectroscopy. *Opt. Express* 18:17699–708
54. Israels B, Albrecht C, Dang A, Barney M, von Hippel PH, Marcus AH. 2021. Sub-millisecond conformational transitions of single-stranded DNA lattices by photon correlation single-molecule FRET. *J. Phys. Chem. B* 125:9426–40
55. Beyerle ER, Dinpahjooh M, Ji H, von Hippel PH, Marcus AH, Guenza MG. 2021. Dinucleotides as simple models of the base stacking-unstacking component of DNA 'breathing' mechanisms. *Nucleic Acids Res.* 49:1872–85
56. Privalov PL, Griko YV, Venyaminov SY. 1986. Cold denaturation of myoglobin. *J. Mol. Biol.* 190:487–98
57. Mikulecky PJ, Feig AL. 2002. Cold denaturation of the hammerhead ribozyme. *J. Am. Chem. Soc.* 124:890–91
58. Mikulecky PJ, Feig AL. 2006. Heat capacity changes associated with nucleic acid folding. *Biopolymers* 82:38–58
59. Vaitiekunas P, Crane-Robinson C, Privalov PL. 2015. The energetic basis of the DNA double helix: a combined microcalorimetric approach. *Nucleic Acids Res.* 43:8577–89

60. Phelps C, Israels B, Jose D, Marsh MC, von Hippel PH, Marcus AH. 2016. Using multi-order time correlation functions (TCFs) to elucidate biomolecular reaction pathways from microsecond single-molecule fluorescence experiments. *J. Phys. Chem. B* 120:13003–16
61. Phelps C, Israels B, Jose D, Marsh MC, von Hippel PH, Marcus AH. 2017. Using microsecond single-molecule FRET to determine the assembly pathways of T4 ssDNA binding protein onto model DNA replication forks. *PNAS* 114:E3612–21
62. Widom JR, Johnson NP, von Hippel PH, Marcus AH. 2013. Solution conformation of 2-aminopurine (2-AP) dinucleotide by ultraviolet 2D fluorescence spectroscopy (UV-2D FS). *New J. Phys.* 15:025028–43
63. Datta K, Johnson NP, Villani G, Marcus AH, von Hippel PH. 2012. Characterization of the 6-methyl isoxanthopterin (6-MI) base analog dimer, a spectroscopic probe for monitoring guanine base conformations at specific sites in nucleic acids. *Nucleic Acids Res.* 40:1191–202
64. Ji H, Johnson NP, von Hippel PH, Marcus AH. 2019. Local DNA base conformation and ligand intercalation in DNA constructs containing optical probes. *Biophys. J.* 117:1101–15
65. Camel BR, Jose D, Meze K, Dang A, von Hippel PH. 2021. Mapping DNA conformations and interactions within the binding cleft of bacteriophage T4 single-stranded DNA binding protein (gp32) at single nucleotide resolution. *Nucleic Acids Res.* 49:916–27
66. Whaley-Mayda L, Guha A, Tokmakoff A. 2022. Resonance conditions, detection quality, and single-molecule sensitivity in fluorescence-encoded infrared vibrational spectroscopy. *J. Chem. Phys.* 156:174202-1-15
67. Raymer MG, Landes T, Marcus AH. 2021. Entangled two-photon absorption by atoms and molecules: a quantum optics tutorial. *J. Chem. Phys.* 155:081501-1-25
68. Landes T, Raymer MG, Allgaier M, Merkouche S, Smith BJ, Marcus AH. 2021. Quantifying the enhancement of two-photon absorption due to spectral-temporal entanglement. *Optics Express* 29:20022–33
69. Landes T, Merkouche S, Allgaier M, Smith BJ, Marcus AH, Raymer MG. 2021. Experimental feasibility of molecular two-photon absorption with isolated time-frequency-entangled photon pairs. *Phys. Rev. Res.* 3:033154-1-9